

# Switching dynamics and critical behavior of standard problem no. 4

R. D. McMichael, M. J. Donahue and D. G. Porter

*National Institute of Standards & Technology, Gaithersburg, MD 20899, USA*

Jason Eicke

*Institute for Magnetism Research, George Washington University, Washington, DC 20052, USA*

We report results for  $\mu$ MAG standard problem no. 4, a  $500 \text{ nm} \times 125 \text{ nm} \times 3 \text{ nm}$  rectangle of material with properties to mimic Permalloy. Switching dynamics are calculated for fields applied instantaneously to an initial s-state: Field 1 at  $170^\circ$  and Field 2 at  $190^\circ$  ( $-170^\circ$ ) from the positive long axis. Reversal in Field 1 proceeds by propagation of end domains toward the sample center. Reversal in Field 2 involves rotation of the end domains in one direction while the center of the particle rotates in the opposite direction, resulting in collapsing  $360^\circ$  walls with complex dynamics on fine length scales. Approaching the static coercivity,  $H_c$ , in small field steps, we find that the ring down frequency,  $f$ , and susceptibility,  $\chi$  are in approximate agreement with a single-spin model that predicts  $f \propto (H_c - H)^{1/4}$  and  $\chi \propto (H_c - H)^{-1/2}$ . We show a correlation between the modes of oscillation that become unstable at the critical field and the switching behavior.

## I. INTRODUCTION

Dynamic micromagnetic computations are increasingly important for rate-sensitive applications such as magnetic memory. There has been an increasing use of numerical micromagnetics to investigate the normal modes of oscillation in micromagnetic structures<sup>1-3</sup>. Standard problem no. 4 was proposed<sup>4</sup> as a benchmark for solutions of the Landau-Lifshitz equations of motion that involves calculating the switching dynamics of a rectangle of magnetic material with material parameters set to mimic Permalloy. The material parameters and dimensions are selected to test the dynamics encountered in switching of MRAM elements, but thermal fluctuations, defects and other forms of disorder are not included.

In section II, we present solutions for two applied fields on standard problem no. 4 for comparison with other solutions<sup>4-6</sup> and we note that for Field 2 the switching dynamics are much more complicated than for Field 1. In section III we use Landau-Lifshitz dynamics to characterize the approach to critical fields. We conclude by noting correlations between the switching behavior and the modes that become unstable at the critical fields.

## II. SWITCHING CALCULATIONS

The dimensions and field orientations for standard problem no. 4 are shown in Fig. 1. The initial state is an equilibrium s-state at zero applied field, and the switching is induced by instantaneous application of one of two fields:

**Field 1**  $\mu_0 H = (-24.6, 4.3, 0.0) \text{ mT}$ ,

**Field 2**  $\mu_0 H = (-35.5, -6.3, 0.0) \text{ mT}$ .

These fields are  $170^\circ$  and  $190^\circ$  from the  $+x$ -axis, approximately double the static critical fields in these directions.

We used the OOMMF public micromagnetic code<sup>7</sup> to compute solutions to standard problem no. 4. The mesh was a 2D square grid with 3D spins interacting through the exchange interaction and magnetostatic fields. Magnetostatic energy was computed under the assumption that the magnetization was uniform within each cell, and the magnetostatic field is averaged over each cell volume<sup>8,9</sup>. Two exchange energy representations were used, an “eight-neighbor dot product” representation and a “four-neighbor angle” representation<sup>10</sup>. The material parameters used were saturation magnetization  $M_s = 8.0 \times 10^5 \text{ A/m}$ , exchange stiffness parameter  $A = 1.3 \times 10^{-11} \text{ J/m}$ , and zero magneto-crystalline anisotropy.

The dynamics of the magnetization were calculated following the Landau-Lifshitz equations of motion,

$$\frac{d\mathbf{M}}{dt} = -|\gamma'|(\mathbf{M} \times \mathbf{H}_{\text{eff}}) - \frac{\lambda}{M_s}(\mathbf{M} \times (\mathbf{M} \times \mathbf{H}_{\text{eff}})) \quad (1)$$

with  $|\gamma'| = 2.21 \times 10^5 \text{ m/As}$  and  $\lambda = 0.02|\gamma'|$ .

The maximum time step was set at 0.2 ps, but smaller time steps were taken as necessary to keep the error within certain bounds<sup>11</sup>. We use the maximum angle between neighboring spins as an indication of how closely our discretized computation approximates Brown’s continuum micromagnetics.

For Field 1, the dynamic response and magnetization pattern during reversal are shown in Fig. 2a. The magnetization rotates counterclockwise everywhere in the particle, most rapidly at the ends, then in the middle as domain walls propagate toward the middle and annihilate. With a 2.5 nm cell size, and eight-neighbor dot product exchange, the maximum angle between neighboring spins was  $22.3^\circ$ .

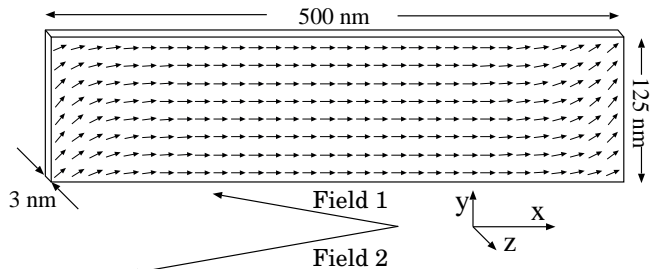


FIG. 1. Dimensions and coordinate system of standard problem no. 4 with the initial s-state displayed and directions and relative magnitudes of the applied fields.

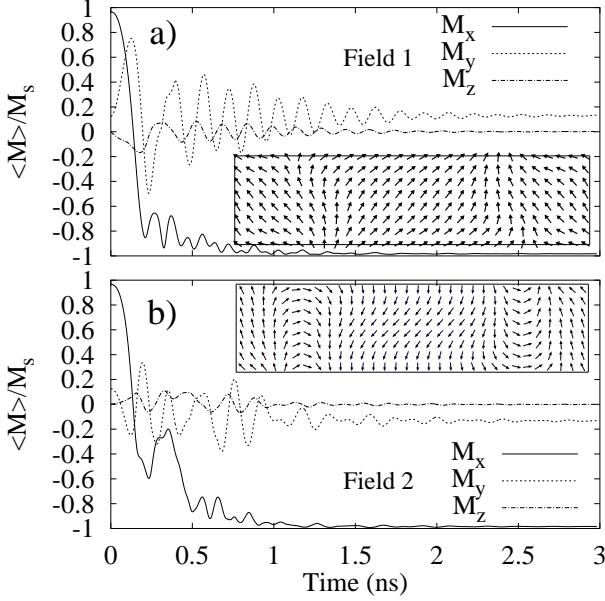


FIG. 2. Spatially averaged magnetization responses and transient magnetization patterns (insets) captured as  $\langle M_x \rangle$  passed through zero for a) Field 1 at 0.138 ns and b) Field 2 at 0.137 ns.

For Field 2, the dynamic response and magnetization pattern during reversal are shown in Fig. 2b. The magnetization initially rotates counterclockwise near the ends, but clockwise in the middle resulting in  $360^\circ$  domain walls and complex dynamics on fine length scales as the  $360^\circ$  walls collapse. We initially used 2.5 nm cell size and the eight-neighbor dot product exchange representation. The maximum angle between neighboring spins was  $71.9^\circ$  at 0.571 ns. Finally, the results shown in Fig. 2b are from a calculation done with 3.125 nm cells using a “four-neighbor angle” exchange energy representation<sup>10</sup> where the maximum angle between spins was reduced to  $48.1^\circ$ . Under this representation, the exchange energy is proportional to the square of the angle between neighboring spins. Unlike the dot product representation, the four-angle has the property of providing an increasingly stronger aligning torque as the angle between spins increases up to  $180^\circ$ .

### III. CRITICAL BEHAVIOR

The behavior of the magnetization near the critical fields in micromagnetic systems has been discussed by several authors including Hubert<sup>12</sup>. In many situations, the critical point is accompanied by a divergence in the susceptibility which can be used to extrapolate calculated results to a critical point. It is shown below that the “slowing down” of the vibrational response that occurs as torques become small near the critical point can also be used to extrapolate the critical field.

As a guide for interpreting the behavior of the magnetization near the critical field, we consider a single domain particle with a field applied along a nearly arbitrary direction, not along one of the symmetry axes of the particle. As the field is swept along this direction,

the equilibrium position of the magnetization will track an energy minimum until that minimum disappears at a critical value of the applied field,  $\mathbf{H}_c$ , where the magnetization will become unstable in a certain direction. Just at the point of instability, we assume that the energy will be of the form

$$E_c = -U\eta^3 + K\nu^2, \quad (2)$$

where  $\eta$ ,  $\nu$ , and  $\zeta$  are Cartesian components of the normalized magnetization in a coordinate system defined such that the  $\zeta$ -axis is directed along the equilibrium magnetization direction at the critical field, and the  $\eta$ -axis points along the direction of instability. This form of the energy has the features expected of a critical point. At the critical point,  $\eta = \nu = 0$ , and the magnetization is stationary, since the gradient of  $E_c$  is zero.  $M$  is stable in the  $\nu$ -direction since  $\partial^2 E_c / \partial \nu^2 > 0$ , but the magnetization is not stable in the  $\eta$ -direction since  $\partial^2 E_c / \partial \eta^2 = 0$ , and  $\partial^3 E_c / \partial \eta^3 \neq 0$ . A plot of  $E_c$  for  $U = K = 1$  is shown in the inset to Fig. 3.

As the applied field approaches a critical value,  $\mathbf{H}_c$ , we define  $\mathbf{h} = \mathbf{H} - \mathbf{H}_c$  with components  $(h_\eta, h_\nu, h_\zeta)$  to be the difference between the applied field and the critical applied field value. Adding the additional Zeeman energy due to  $\mathbf{h}$ , the energy is

$$E = E_c - \mu_0 M \left[ h_\eta \eta + h_\nu \nu + h_\zeta \left( 1 - \frac{\eta^2}{2} - \frac{\nu^2}{2} \right) \right] \quad (3)$$

where higher order terms in the small quantities  $\eta, \nu$  and  $\mathbf{h}$  are neglected.

The equilibrium value of  $\eta$  is given by

$$\eta_{\text{eq}} = \frac{\mu_0 M}{6U} \left[ h_\zeta - \sqrt{(h_\zeta)^2 - \frac{12U h_\eta}{\mu_0 M}} \right], \quad (4)$$

and the divergent susceptibility tensor element  $\chi_{\eta,\eta}$  is

$$\chi_{\eta,\eta} = M \frac{\partial \eta_{\text{eq}}}{\partial h_\eta} = M \left[ h_\zeta^2 - \frac{12U}{\mu_0 M} h_\eta \right]^{-1/2}. \quad (5)$$

In the special case where  $h_\eta = 0$ , for example when  $\mathbf{h}$  is parallel to  $\mathbf{M}$  at the critical field, the susceptibility is proportional to  $h_\zeta^{-1}$ . Otherwise, for small  $|\mathbf{h}|$ ,  $h_\zeta^2 \ll 12U h_\eta / \mu_0 M$  and the susceptibility diverges proportional to  $h_\eta^{-1/2}$ .

The frequency of precession about the equilibrium position depends on the curvature of the energy surface at the equilibrium position<sup>13</sup>:

$$f = \frac{\sqrt{\gamma'^2 + \lambda^2}}{2\pi \mu_0 M} \left[ \frac{\partial^2 E}{\partial \eta^2} \frac{\partial^2 E}{\partial \nu^2} - \left( \frac{\partial^2 E}{\partial \eta \partial \nu} \right)^2 \right]^{1/2} \bigg|_{\eta_{\text{eq}} \nu_{\text{eq}}}. \quad (6)$$

Using (3) and (4) the precession frequency is

$$f = \frac{\sqrt{\gamma'^2 + \lambda^2}}{2\pi} \left[ h_\zeta + \frac{2K}{\mu_0 M} \right]^{1/2} \left[ h_\zeta^2 - \frac{12U}{\mu_0 M} h_\eta \right]^{1/4}. \quad (7)$$

In the special case where  $h_\eta = 0$ , the resonant frequency is proportional to  $h_\zeta^{1/2}$ . Otherwise, for small  $|\mathbf{h}|$ ,  $h_\zeta^2 \ll$

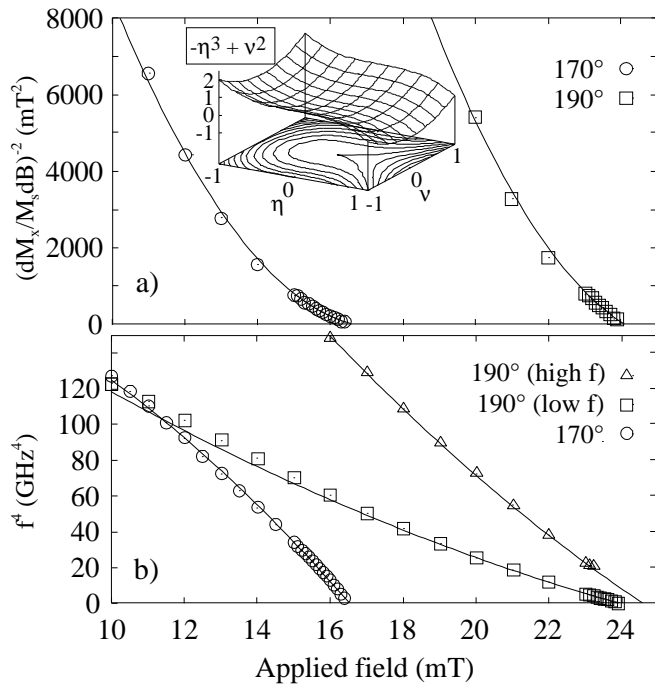


FIG. 3. a) The inverse susceptibility squared and b) the fourth power of the resonance frequency calculated from the magnetization response as the field was stepped toward the critical fields. Lines are quadratic fits to the data. Inset: the form of the energy,  $E_c(\eta, \nu)$ , for a single spin at the critical point plotted for  $U = K = 1$ .

$12U h_\eta / \mu_0 M$  and the resonant frequency is proportional to  $h_\eta^{1/4}$ .

We compared the predictions of this single spin model to the response of the magnetization to fields stepped toward the critical field along the directions of Field 1 ( $170^\circ$ ) and Field 2 ( $190^\circ$ ). The equilibrium magnetization values were used to calculate  $\chi$  and the power spectrum of the ringdown response to each field step was used to determine  $f$ .

Plots of the computed inverse susceptibility squared ( $[dM_x/(M_s dB)]^{-2}$ ) are shown in Fig. 3a. Susceptibility following  $\chi \propto (H_c - H)^{-1/2}$  would appear as a straight line on this plot. The solid lines in Fig. 3a are fits to functions of the form  $a(H - H_c) + b(H - H_c)^2$  with data weighted to reflect uncertainty as a constant percentage of the susceptibility value. The fits used only data within 6 mT of the critical field. The fits extrapolate to critical fields of  $(16.60 \pm 0.02)$  mT and  $(24.08 \pm 0.02)$  mT for fields applied at  $170^\circ$  and  $190^\circ$  respectively. Stated uncertainties indicate the quality of the fit.

The fourth power of the ringdown frequency is plotted in Fig. 3b. Straight lines are expected for  $f \propto (H_c - H)^{1/4}$  behavior. For fields applied at  $190^\circ$ , two peaks are observed in the power spectrum indicating two normal modes of oscillation. The solid lines in Fig. 3b are quadratic fits to the frequency data within 6 mT of the critical fields, weighted to reflect constant uncertainty in the frequency. This uncertainty is consistent with power spectrum peak widths that varied slowly with applied field. The fits to data extrapolate to  $(16.542 \pm 0.005)$  mT for  $170^\circ$  and  $(23.964 \pm 0.004)$  mT and  $(24.62 \pm 0.07)$  mT

for the low and high  $f$  peaks respectively with the field at  $190^\circ$ .

While it is not clear that a single spin model should have any predictive power for the behavior of a nonuniformly magnetized particle, the single spin may have more legitimacy as a model for a *single normal mode* of the particle. The ratio  $a/b$  of the linear and quadratic fit parameters provides an indication of the range over which the system follows the predictions of the single spin model, and these ratios are roughly an order of magnitude larger for the frequency fits (Fig. 3b) than they are for the susceptibility fits (Fig. 3a). While the frequency data track the response of individual normal modes separated by frequency, the susceptibility is a superposition of the response of all the normal modes, and as such is less likely to behave like a single spin.

Comparing the linear response near the critical field to the observed switching behavior, we tentatively associate the normal modes with the ends and center of the particle<sup>1</sup>. Because the switching is initiated by rotation in the ends of the particle in Field 1, we associate the oscillations observed for fields at  $170^\circ$  with the ends of the particle. The low  $f$  mode at  $190^\circ$  and the mode at  $170^\circ$  are the same mode at zero field. We therefore also associate the lower frequency mode for fields along  $190^\circ$  primarily with the particle ends. For 36.1 mT applied at  $190^\circ$  (Field 2) both of the oscillation modes observed for  $190^\circ$  fields would be unstable. Perhaps as a result of this dual instability, the switching in Field 2 is more complicated, starting with magnetization rotating in opposite directions at the ends of the particle with instability of the low  $f$  mode and in the center of the particle with instability of the high  $f$  mode.

- <sup>1</sup> O. Gerardin, H. Le Gall, M. J. Donahue and N. Vukadinovic, these proceedings.
- <sup>2</sup> G. M. Moore, R. L. Stamps, and R. Street, IEEE Trans. Mag., **35**, 3790, (1999).
- <sup>3</sup> N Vukadinovic, O. Vacus, M. Labrune, O. Acher and D. Pain, Phys. Rev. Lett., **85**, 2817 (2000).
- <sup>4</sup> R. D. McMichael, Jason Eicke and M. J. Donahue, <URL: <http://www.ctcms.nist.gov/~rdm/mumag.html>>.
- <sup>5</sup> V. Tsiantos, D. Suess, T. Schrefl, and J. Filder, these proceedings.
- <sup>6</sup> G. Albuquerque, A. Thiaville, J. Miltat, these proceedings.
- <sup>7</sup> M. J. Donahue and D. G. Porter, <URL: <http://math.nist.gov/oommf/>>.
- <sup>8</sup> A. J. Newell, W. Williams, and D. J. Dunlop, J. Geophys. Res. **98** 9551 (1993).
- <sup>9</sup> M. J. Donahue, D. G. Porter, R. D. McMichael, and J. Eicke, J. Appl. Phys., **87**, 5520, (2000).
- <sup>10</sup> M. J. Donahue and R. D. McMichael, Physica B, **233**, 272 (1997).
- <sup>11</sup> M. J. Donahue and D. G. Porter, NIST Interagency Report, NISTIR 6376; <URL: <http://math.nist.gov/oommf/doc>>.
- <sup>12</sup> A. Hubert and W. Rave, Physica Status Solidi B, 211, 815 (1999).
- <sup>13</sup> J. Smit and H.G. Beljers, Philips Res. Rep. **10**, 113 (1955).